Chapter-4

CoS Nano-Spheres: A Pseudocapacitive Electrode for Hybrid Supercapacitors

Chapter-4

CoS Nano-Spheres: A Pseudocapacitive Electrode for Hybrid Supercapacitors

4.1 Introduction

Owing to their excellent electrical conductivity, strong thermal and mechanical stability, rich redox reactions that occur during electrochemical processes, and the ability to enhance ion transport through sulphur, transition metal sulfides (TMS) have recently garnered interest and emerged as a promising alternative to oxide materials for supercapacitors. Nanostructured TMS brings the benefits of cost-effectiveness and higher specific capacitances when compared to their oxide counterparts. TMS now belongs to a novel class of pseudocapacitive material with a wide range of potential applications. [1-5] Recently, single-phase β-NiS nanocrystallites were shown as a superior intercalative redox-mediated pseudocapacitive electrode in the aqueous electrolyte to be utilized as an electrode in hybrid supercapacitors. [6] Similarly, cobalt sulfide compounds with different stoichiometric compositions such as CoS_2, CoS, Co_9S_8 and $Co_{1-x}S$ have attracted significant attention due to their physical, chemical, electronic and optical properties and their vast potential applications in catalysis and electrochemical supercapacitors. [7, 8] The diverse crystal structures of cobalt sulfide, such as hexagonal (CoS), cubic (CoS_2) and densely packed cubic (Co_9S_8) provide the unique chemical characteristics. [9] The synthesis of nanostructured cobalt sulfide, including nanotubes [10], nanosheets [11], spheres [12] and floral [13] forms, significantly increases the specific capacitance.

The chapter describes the synthesis procedure, characterizations and

electrochemical performances of the single-phase hexagonal CoS nano-spheres. The UV-visible and Raman spectra provides evidence of the quantum size phenomenon observed in the CoS nanosphere and validates the nanocrystalline characteristics of the particles. The CoS electrode demonstrates excellent capacitance equivalent to 776 F/g at 1 mV/s and a specific capacitance of 761 F/g at 1 A/g in 2 M KOH aqueous electrolyte. An aqueous asymmetric hybrid supercapacitor (HSC) was assembled with cobalt sulfide (CoS) as the positive electrode and activated carbon (AC) as the negative electrode. The assembled aqueous HSCs with excellent cycling stability resulted in a high energy density of 139.7 Wh/kg and a power density of 7.5 kW/kg are reported here.

4.2 Experimental:

4.2.1 Synthesis Method

Cobalt (II) chloride hexahydrate ($CoCl_2.6H_2O$) (0.1 M, 5.95 g) was dissolved in 250 ml of deionized water for 5 to 6 hours with constant stirring to create a homogenous solution. Subsequently, H_2S gas was passed into the solution using the Kipp generator method. The Co^{2+} and S^{2-} ions released by hydrolysis of $CoCl_2.6H_2O$ and H_2S reacted to form a fine black precipitate of CoS. With the reaction proceeding, the tiny nuclei aggregated into spherical

$$CoCl_2.6H_2O + 2H_2O \rightarrow Co^{2+}(aq) + 8H_2O + 2Cl^-(aq) \quad (4.1)$$

(Co^{2+} solubility step)

+

$$H_2S + 2H_2O \rightarrow 2H_3O^+ + S^{2-} \quad (4.2)$$

H_2S mediated precipitation

$$Co^{2+}(aq) + 8H_2O + 2Cl^-(aq) + 2H_3O^+ + S^{2-} \rightarrow CoS + 2HCl + 10H_2O \quad (4.3)$$

CoS. The black precipitate was then filtered and washed several times with deionized water. The products were dried in a hot air oven (under an N_2 atmosphere) at 120 °C for 24 hours and used for crystallographic and electrochemical characterizations. The mechanism of synthesis is depicted above in equation 4.1 to 4.3.

4.3 Results and Discussions:

4.3.1 XRD Studies

The pre-heated powder sample's XRD pattern demonstrates the purity of the phase and confirms the precipitation of single-phase hexagonal CoS nano-spheres. Rietveld refined XRD plot of hexagonal CoS is shown in Fig. 4.1a. In the space group- P63/mmc with a goodness of fit (χ^2) of 1.16, 14 parameters were refined for CoS nano-spheres.

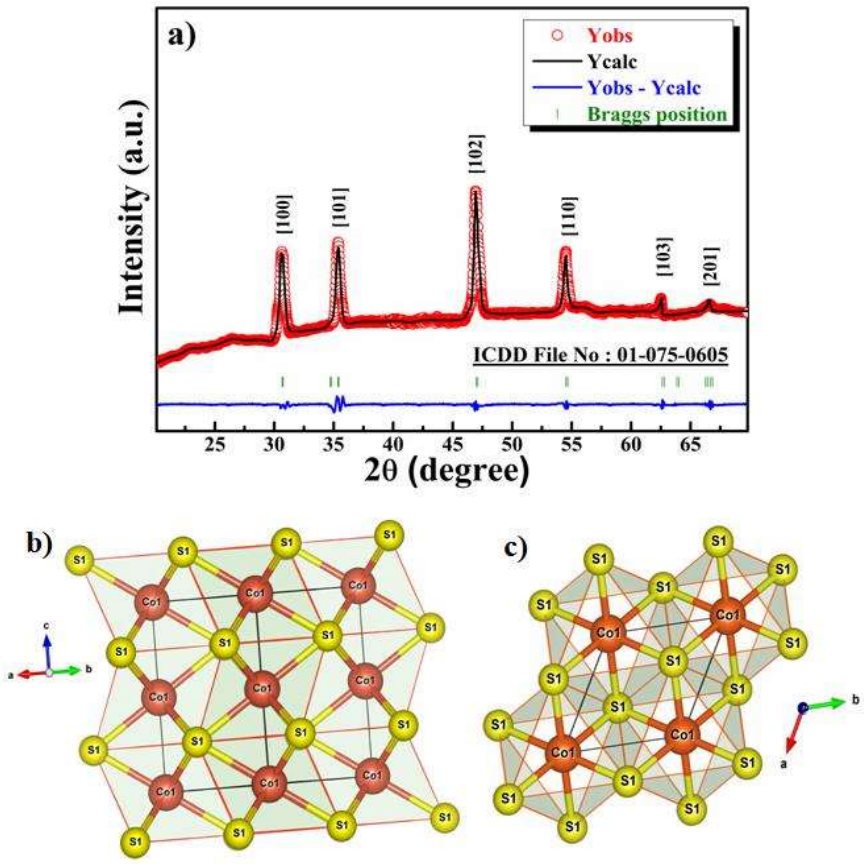

Fig. 4.1 (a) Rietveld refined XRD profile of CoS nano-sphere, **(b)** and **(c)** VESTA image of CoS nano-sphere.

The (100), (101), (102), (110), (103) and (201) planes are represented by the distinct, sharp and prominent diffraction peaks at 2θ values 30.67, 35.35, 46.98, 54.52, 62.63 and 66.67, respectively, of CoS nano-sphere in the hexagonal cell (space group: P63/mmc) with lattice parameters a = b = 3.36 (1) Å, c = 5.16 (3) Å, α = β = 90º and γ = 120º matches very well with the diffraction peaks reported elsewhere (ICDD File No: 01-075-0605). The VESTA image of the CoS nano-sphere in a layered hexagonal structure is shown in Fig. 4.1(b & c).

4.3.2 Thermal Analysis

The as-precipitated black powder (without any pre-heating) was utilized for Thermogravimetric analysis (TGA) under the N_2 atmosphere to understand the thermal stability of the CoS nano-sphere (in Fig. 4.2a). The black powder was heated from room temperature to 700 °C at a rate of 10 °C min^{-1}. There were two stages of weight loss for the CoS nano-sphere. The removal of residual moisture and water trapped between the layers of the CoS nanostructure showed the first stage of weight loss in the temperature range of 200 °C (4.56% weight loss). From 200 to 445 °C, the sample is almost stable with a slight weight loss. After 450 °C, there is a sudden weight loss because of the decomposition of the CoS nano-sphere with the evolution of sulfur. The inset of Fig. 4.2a shows DTA (differential thermogravimetric analysis) plot that clearly shows two peaks. One at 205 °C is due to the desorption of the adsorbed/trapped water molecule while the peak at 535 °C is attributed to the gradual loss of sulfur and structural collapse (a weight loss of ~10%). The weight loss is slow up to 450 °C which implies that the CoS nano-sphere is stable to a fairly high temperature. [14], [15]

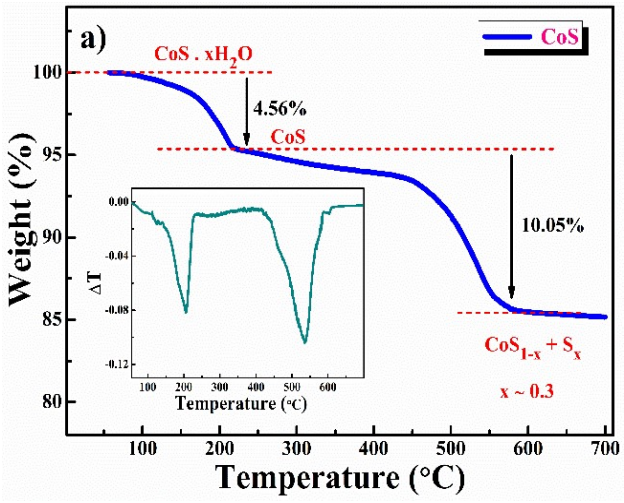

Fig. 4.2 (a) TGA plot of CoS nano-sphere in an N_2 atmosphere (DTA plot in the inset)

4.3.3 Structural Analysis

FT-IR spectrum of the as-prepared (without preheating) CoS nano-spheres is shown in Fig. 4.2b. The stretching vibrations which correspond to the OH groups of adsorbed water on the surface showed a broad peak at 3390 cm^{-1}. [16] Two peaks at 1225 and 1664 cm^{-1} indicate the bending vibration of sulfonated (S-O) groups and the bending vibration of absorbed H_2O in CoS, respectively. The bands at 404, 415 and 433 cm^{-1} are related to the symmetrical stretching vibration whereas 1048 cm^{-1} is related to the asymmetrical stretching vibration assigned to Co-S bonds in sulfides. A further small

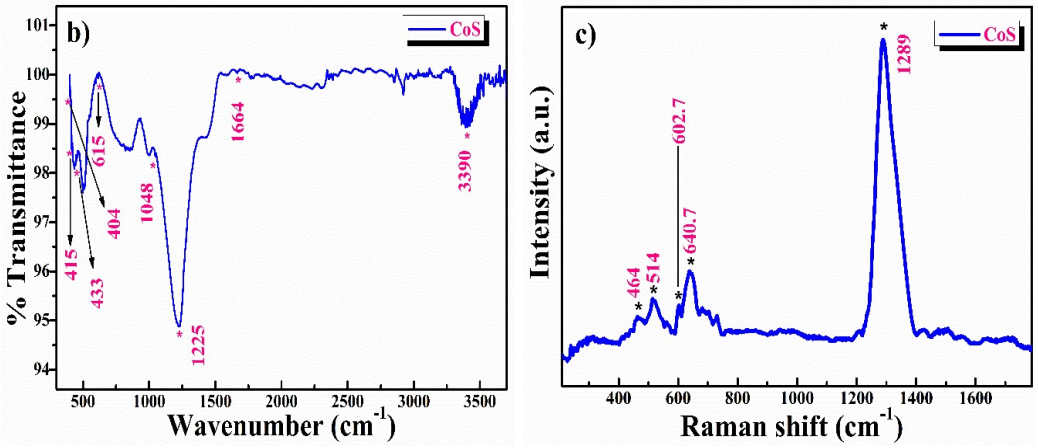

Fig. 4.2 (b) FT-IR spectra and, **(c)** Raman spectra of CoS nano-spheres

peak at 615 cm^{-1} is related to the stretching vibration of Co atoms in the surface of the CoS nano-sphere which is in fair agreement with results published elsewhere. [17]

For additional studies on the CoS structure, a standard Raman scattering spectrum shown in Fig. 4.2c was performed on pre-heated active material (CoS). Peaks at 464, 514, 603 and 641 cm^{-1}, which correspond to the typical phonon modes E_g, F_{2g}^1, F_{2g}^2 and A_{1g} respectively for CoS nano-sphere, have been detected. [18-20] The peaks at 641 cm^{-1} are due to the S-S (involved) stretching vibration and 464, 514 and 603 cm^{-1} were attributed to the vibration of the Co-S bond. Due to the quantum confinement of optical phonons, Raman lines for the CoS nano-sphere were shifted toward lower wave numbers, i.e., bathochromic shift or red-shift indicating the phonon confinement effect supported by the high-intensity stretching band at 1289 cm^{-1}. [21]

4.3.4 Bandgap Measurement and Surface Area Analysis

To study the optical characteristics of the as synthesized pre-heated CoS nano-sphere, UV-visible spectra was measured at room temperature (Fig. 4.2d). The absorbance peak observed at 368 nm indicates the formation of CoS nano-spheres which is in accordance with literature. [22] The optical band gap of the CoS nano-sphere was calculated with the help of the Tauc plot (inset of Fig. 4.2d) which was found to be 2.44 eV. The increase in the band gap could be due to the decrease in the crystallite size, which is in fair agreement with the Raman spectra and XRD results. [17]

The BET surface area plot shown in Fig. 4.2e represents a complex blend of micro- and mesoporous structures of CoS nanospheres and the adsorption and desorption isotherms show type IV isotherm properties. The calculated BET-specific surface area is 13.7 m^2/g and the average diameters of pores are 14.54 nm. The mesoporous nature and high surface area of the CoS nano-spheres provides superior contact with the electrolyte and

enhance the electrochemical kinetics, as OH^- ions in an aqueous KOH electrolyte are substantially smaller than the mesopore diameter of CoS nanospheres. [23], [24]

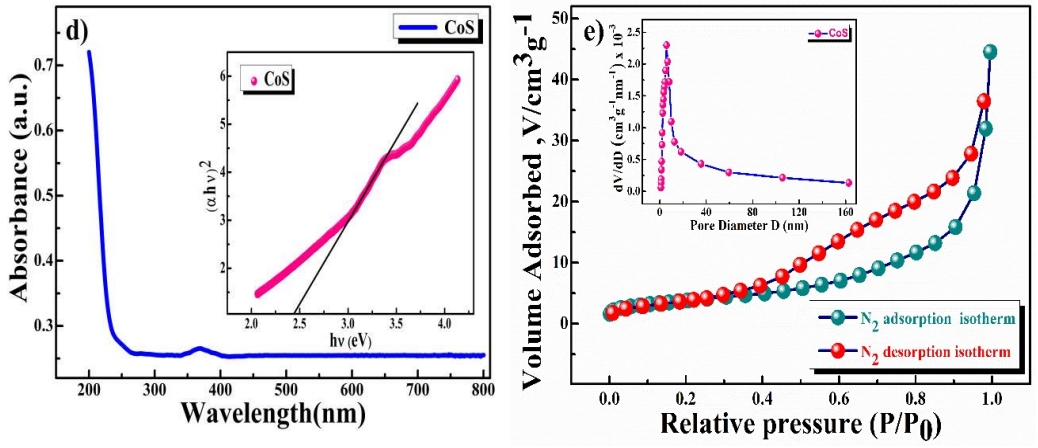

Fig. 4.2 (d) UV-Visible spectra (Tauc plot in the inset) and **(e)** BET surface area plot using nitrogen adsorption/desorption isotherm of CoS nano-sphere.

4.3.5 XPS Analysis

The elemental composition and oxidation state of the CoS nano-sphere were studied using X-ray photoelectron spectroscopy (XPS). The high-resolution Co (2*p*) spectrum, Fig. 4.3a, shows $2p_{3/2}$ and $2p_{1/2}$ at 781.0 and 796.7 eV, and the corresponding satellite peaks at 785.7 and 802.3 eV are assigned to Co^{2+} oxidation state. The high-resolution S (2*p*) spectrum, in Fig. 4.3b, shows two characteristic peaks at 162.7 and 161.6 eV,

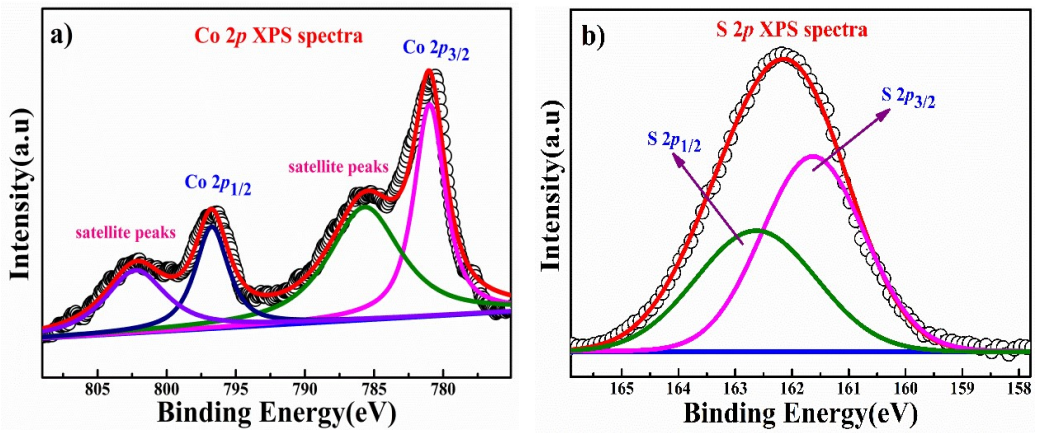

Fig. 4.3 Deconvoluted XPS plot of CoS nano-sphere, **(a)** Co (2*p*) spectra, and **(b)** S (2*p*) spectra

respectively. The peak observed at 161.6 eV corresponds to S ($2p_{3/2}$) associated with the Co-S bonding and the peak that appeared at 162.7 eV corresponds to S($2p_{1/2}$) and is attributed to the surface bonding of divalent sulfur. [25], [26]

4.3.6 FE-SEM and HR-TEM Analysis

SEM image (Fig. 4.4a). The SEM image depicts the agglomerated sub-micron-sized grains. The EDX (energy dispersive x-ray) analysis image presented in Fig. 4.4b confirms the material's elemental composition. Fig. 4.4c shows the HRTEM image demonstrating the successful formation of CoS nanospheres. The nanosphere with an average diameter of 67 nm, exhibits localized atomic arrangements across the sample. The selected area electron diffraction (SAED) pattern, in Fig. 4.4d, displays distinct, well-aligned diffraction spots with lattice spacing 0.29, 0.25, 0.19 and 0.17 nm for (100), (101), (102) and (110) planes respectively. The lattice fringes of the CoS nano-sphere are seen in Fig. 4.4e demonstrating the crystalline nature of the nanoparticles. An FFT (fast fourier transform) and an inverse FFT image of a CoS nano-sphere, as determined using Image-J software, are shown in the inset (i and ii) of Fig. 4.4e. The d-spacing value was found to be 0.29 nm which matches reasonably with the (100) plane of the CoS nano-sphere.

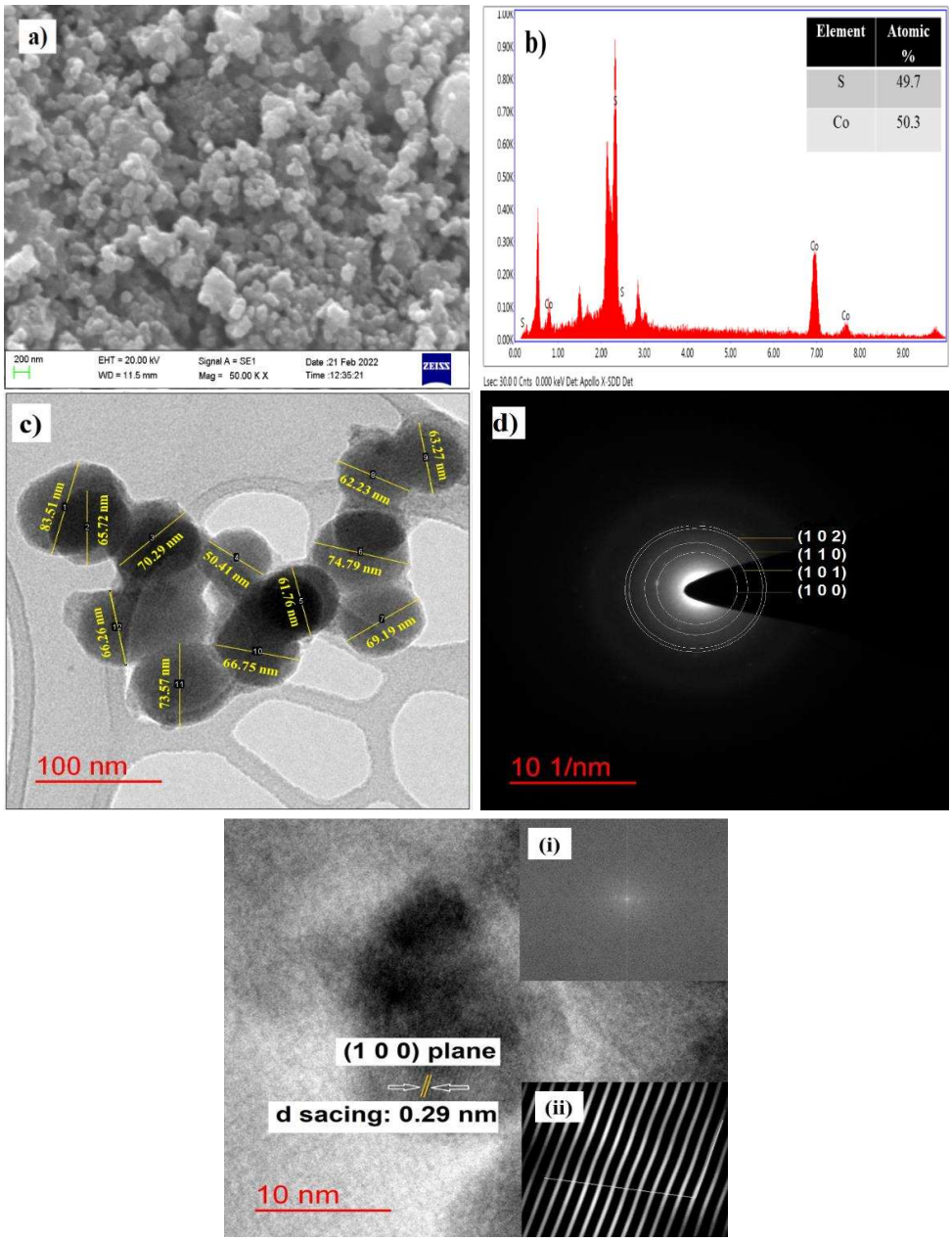

Fig. 4.4 (a) FE-SEM **(b)** EDX image of the prepared CoS nano-sphere, **(c)** HRTEM images of CoS nano-sphere, **(d)** SAED pattern shows diffused ring pattern for lattice plane diffractions, (e) Lattice fringes representing (100) plane of CoS nano-sphere. The inset (i and ii) of **(e)** with FFT, inverse FFT images.

4.3.7 Electrochemical Studies:

4.3.7.1 Cyclic Voltammetry Analysis

The electrochemical behavior was examined using cyclic voltammetry and

galvanostatic charge-discharge to determine the materials' applicability for energy storage as supercapacitors. The capacitive charge-storage properties of the CoS electrodes were first evaluated by CV using the three-electrode assembly where the CoS nano-sphere was deployed as a working electrode, the platinum electrode as the counter electrode, and saturated Hg/HgO (1 M KOH) as a reference electrode. The CV curves were measured at different concentrations of aqueous KOH electrolyte, namely concentrations of 0.5, 1, 2, and 4 M. Electrolyte concentration vs. mass-specific capacitance plot is presented in Fig. 4.5a. The specific charge storage capacitances using equation 4.4 were found to be 541, 644, 776, and 726 F/g at the scan rate of 1 mVs^{-1} in 0.5, 1, 2, and 4 M concentration of KOH electrolyte.

The specific capacitance increase with the increase in OH^- concentration and reaches to the highest capacitance at 2 M KOH electrolyte and then decreases with a further increase in the OH- concentration. [27]

$$\boldsymbol{C} = \frac{\int_{E_1}^{E_2} \boldsymbol{i}\,(\boldsymbol{E})\boldsymbol{dE}}{\boldsymbol{2\,m\,v\,(E_2 - E_1)}} \qquad (4.4)$$

where C is the capacitance in F/g, $(E_2 - E_1)$ is the operating potential window (V), the integral $\int_{E_1}^{E_2} i\,(E)dE$ is the total voltammetric charge stored in both positive and negative sweeps in the CV plot.

The capacitance values in the forward and reverse directions do not precisely match; however, for the holistic picture, we have taken the average value hence the factor 1/2 is used, where *i(E)* is the obtained current (A), *m* is the mass (g) of CoS nanosphere,

and v is the operative scan rate (V s^{-1}). The CV curve shown in Fig. 4.5d using 2 M KOH electrolyte shows two pairs of well-separated redox peaks, indicating that the electrochemical capacitance of the CoS electrode mainly results from the

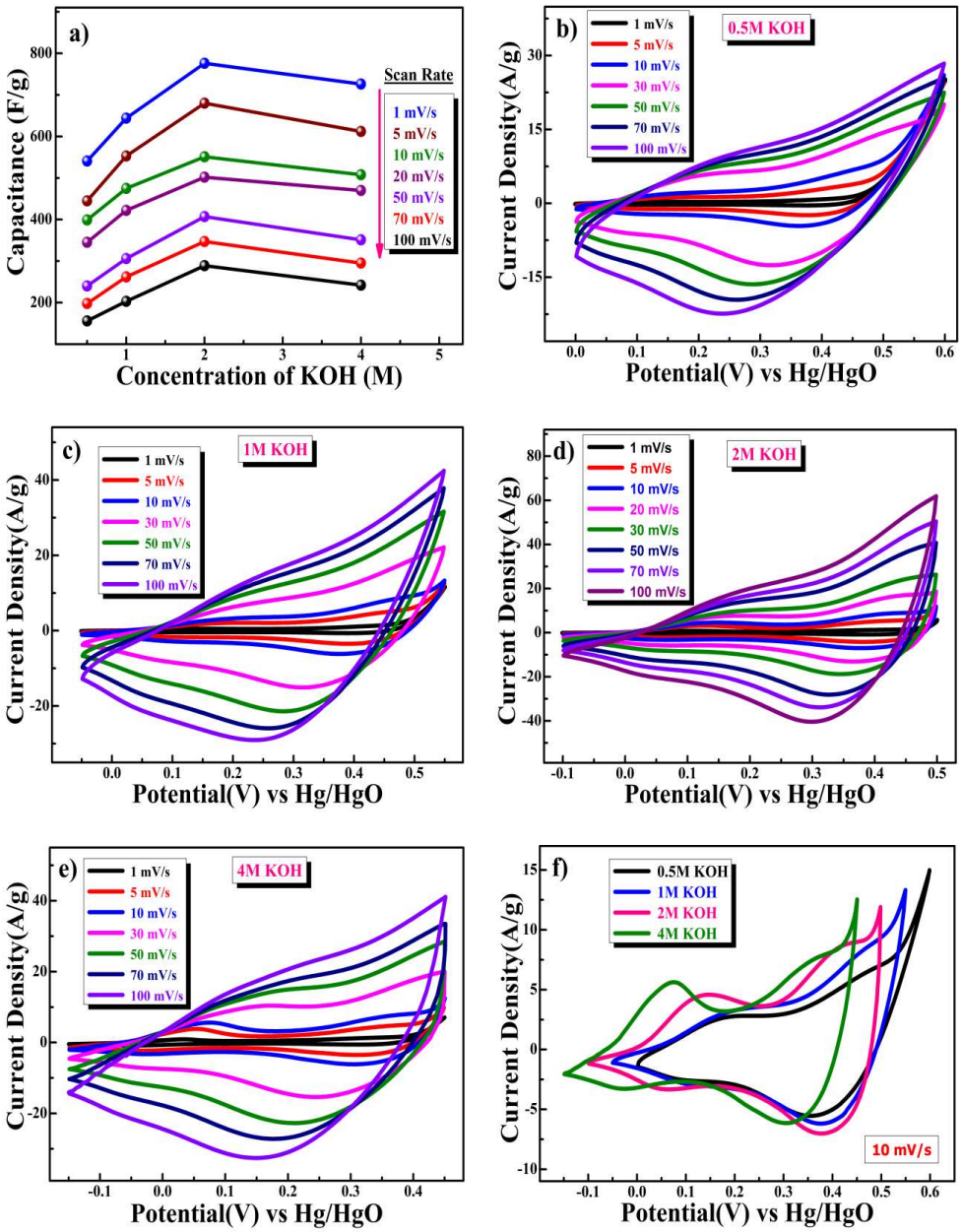

Fig. 4.5 (a) Plot of KOH concentrations vs. specific capacitance at different scan rates. Typical CV curves for CoS electrode in **(b)** 0.5, **(c)** 1, **(d)** 2 and **(e)** 4 M KOH solutions at different scan rates of 1-100 mVs^{-1}. **(f)** Comparative CV study in different concentrations of electrolytes at 10 mV/S.

pseudocapacitance rather than the electric double-layer capacitance. As can be observed, non-rectangular and quasi-reversible curves were obtained in the potential range of -0.1 – 0.5 V indicating a pseudo-capacitive behavior coupled with surface redox (electrosorption). [28] Even at higher scan rates, the shape of the CV curves remained identical, indicating excellent charge transfer stability.

As represented in equation 4.5, redox peaks arise due to the reversible interconversion of $Co^{2+} \rightleftharpoons Co^{3+}$ through electrosorption (redox) of OH^- ions coupled with EDLC-type surface contribution of capacitance as given in equation 4.6. [15]

$$Co^{2+}S + OH^- \rightleftharpoons Co^{3+}SOH + e^- \qquad (4.5)$$

$$Co^{2+}S + xK^+OH^- \rightleftharpoons K^+_xCo^{2+}S(OH^-)_x \qquad (4.6)$$

The net charge storage capacitance of the electrode can be represented as equation 4.7.

$$Co^{2+}S + xK^+OH^- + OH^- \rightleftharpoons K^+_xCo^{2+}S(OH^-)_{1+x} \qquad (4.7)$$

Typical CV curves for the CoS electrode are shown at 0.5, 1 and 4 M KOH solutions in Fig. 4.5 (b) 0.5, (c) 1 and (e) 4 M respectively at various scan rates from 1 to 100 mVs^{-1}.

Capacitance was found to be 776, 680, 551, 502, 463, 407, 347 and 289 F/g at scan rates of 1, 5, 10, 20, 30, 50, 70 and 100 mVs^{-1} respectively in 2 M KOH electrolyte. As the active surface areas of the electrode are more accessible for electrochemical interactions at lower scan rates, the specific capacitance decrease at higher scan rates. The redox peak positions shifted linearly with the increase in the scan rate. The anodic peak potential shifted to a higher value while the cathodic peak potential shifted to a lower voltage. This may be due to the sluggish charge transfer kinetics which is the limiting step of the reaction.

The comparative CV study in different concentrations of electrolytes ranging from 0.5 to 4 M (in Fig. 4.5f) at 10mV/s depicts that the redox potential is moved towards a lower voltage with increasing concentration of the electrolyte KOH which is undesirable for high-voltage applications. Further, current density values also suggest an increase in capacitance of the electrode from 0.5 to 2 M KOH concentration of the electrolyte and a decrease in capacitance for higher KOH concentrations. [24]

4.3.7.2 Determination of Diffusion Coefficient

Fig. 4.5g shows the anodic and cathodic peak currents in linear relation with the square root of scan rate ($\upsilon^{1/2}$) suggesting that the CV curve presents a semi-infinite diffusion-controlled charge storage. Determining the diffusion coefficient will also help understand electrode diffusion dynamics. The diffusion coefficient for OH^- ions in the electrode was measured with the help of the Randles-Sevick equation shown in equation 4.8. [29]

$$i_p = 2.686 \times 10^5 \times n^{3/2} A\, D^{1/2}\, C_o\, v^{1/2} \qquad (4.8)$$

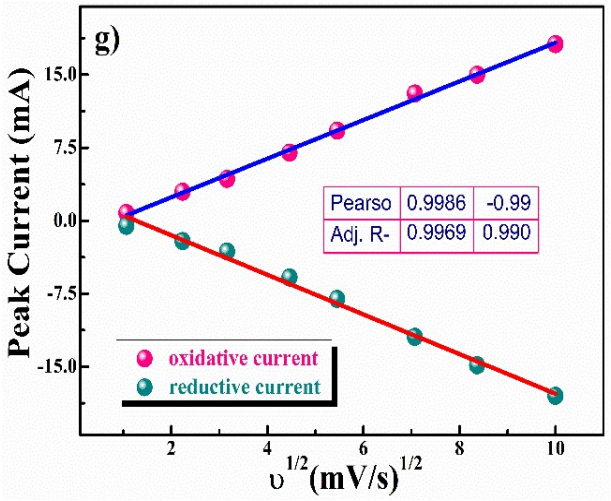

Fig. 4.5 (g) Plot of peak current vs. square root of the scan rate for diffusion kinetics for the CoS electrode.

Where i_p is peak current (A), n is the number of electrons transferred in the redox process (n~1), A is the area of the electrode in cm^2, D is the diffusion coefficient of OH^- ion in cm^2/s, C_o is the concentration of electrolyte (OH^- ion) in mol/cm^3, υ is the scan rate in V/s. D of OH^- ions diffusion in the electrode was found to be 2.16×10^{-9} cm^2/s for oxidation and $0.96\times10^{-9}cm^2/s$ for reduction process.

4.3.7.3 Kinetics Studies (Determination of *b* values) and Dunn's Plot Analysis

The different charge storage kinetics/mechanisms of the CoS electrode were evaluated qualitatively using the power law described in equation 4.9. [30]

$$i = av^b \qquad (4.9)$$

Where i is the current (A), values of a & b are adjustable parameters, and v is the sweep rate (V/s). In general, the b value exists between 0.5-1 and b = 1 stand for the surface control capacitance or electrosorption, while b = 0.5 stands for the semi-infinite diffusion control process for intercalative battery type behavior. [31] From Fig. 4.6a, the b values were calculated from the corresponding log (v) versus log (i) plots and were found to be 0.68 and 0.77 for oxidative and reductive current scan respectively, suggesting that currents originate mainly from surface capacitive reactions rather than from diffusion-controlled insertion reactions. The specific capacitance of the CoS nano-sphere is attributed to both surface-controlled redox-mediated pseudocapacitance and semi-infinite diffusion-controlled processes. Trasatti's [32] and Dunn's [33] methods were employed to calculate the contributions of diffusion-controlled and redox-mediated (non-diffusion-controlled) capacitance. The voltammetry scan rate dependency, shown in Fig. 4.6b, demonstrates the capacitive contribution to the current response.

The current response at fixed potential results from the contributions of two separate

mechanisms, diffusion-controlled insertion or intercalation and surface capacitive reactions.

$$i(\upsilon) = k_1\upsilon + k_2\upsilon^{1/2} \qquad (4.10)$$

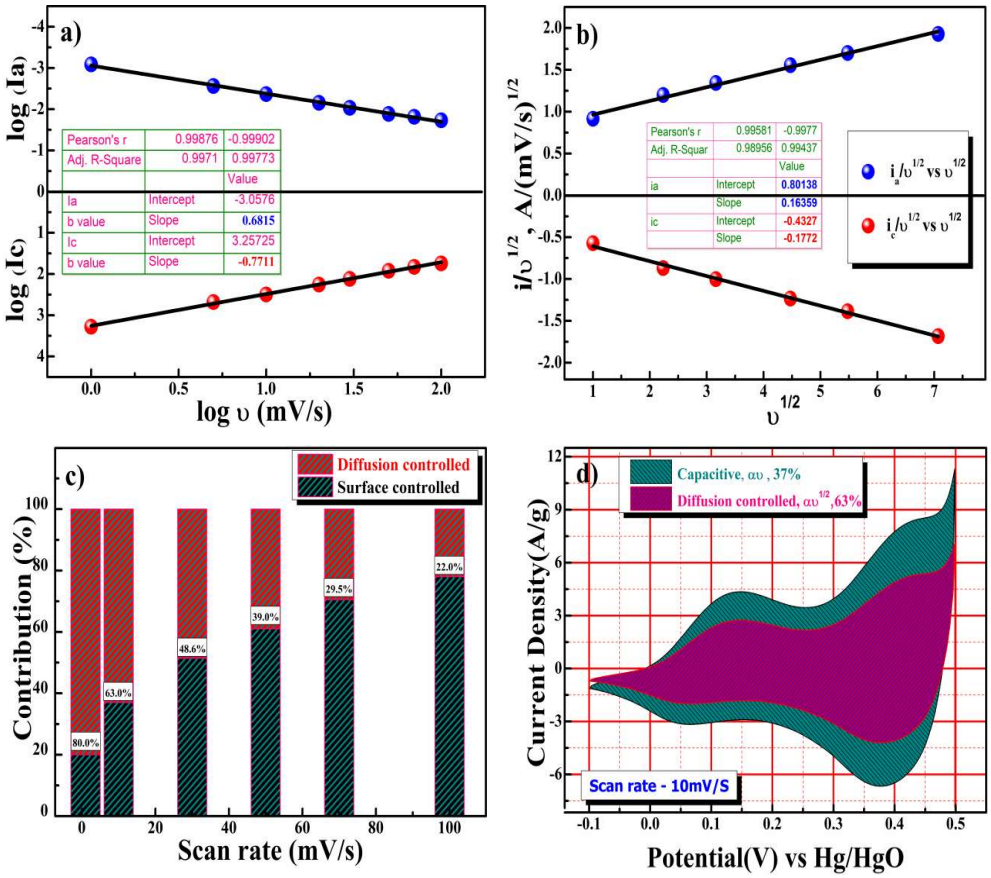

Fig. 4.6 Electrochemical kinetics of the CoS electrode **(a)** Plot of between log (peak current) vs. log (scan rate) at two different scan rate regions, **(b)** Plot of the power law at charged state and discharged state, **(c)** Diffusive and capacitive contribution of the electrode at different scan rates and **(d)** Capacitance contribution at 10 mVs^{-1}

For better understanding, eq. 4.10 was modified as

$$\frac{i(\upsilon)}{\upsilon^{1/2}} = \frac{k_1}{\upsilon^{1/2}} + k_2 \qquad (4.11)$$

In eq. 4.10, $k_1\upsilon$ and $k_2\upsilon^{1/2}$ are the current contributions of both the surface capacitance and diffusion-controlled intercalation. Thus, the determination of k_1 and k_2 using the slope and intercept of the y-axis from linear fit can result in the contribution of surface

capacitance and diffusion-controlled intercalation to the current density at fixed specific potentials. [34] {(V)/$\upsilon^{1/2}$vs. $\upsilon^{1/2}$} plot shown in Fig. 4.6c presents the contribution of surface capacitance and diffusion-controlled intercalation process at different sweep rates. Fig. 4.6d represents the contribution of both surface capacitance and diffusion-controlled intercalation processes at the scan rate of 10 mVs^{-1} and the surface capacitance or electrosorption was found to be 37% and the contribution of diffusion-controlled intercalation was found to be ~63%.

4.3.7.4 Trassati's Plot Analysis

Trasatti plot was used to examine the charge stored in the outer and inner surfaces of the electrode. The electrode's inner and outer surface capacitances result the total specific capacitance. It can be represented as

$$C_{Total} = C_{in} + C_{out}(\text{F/g}) \qquad (4.12)$$

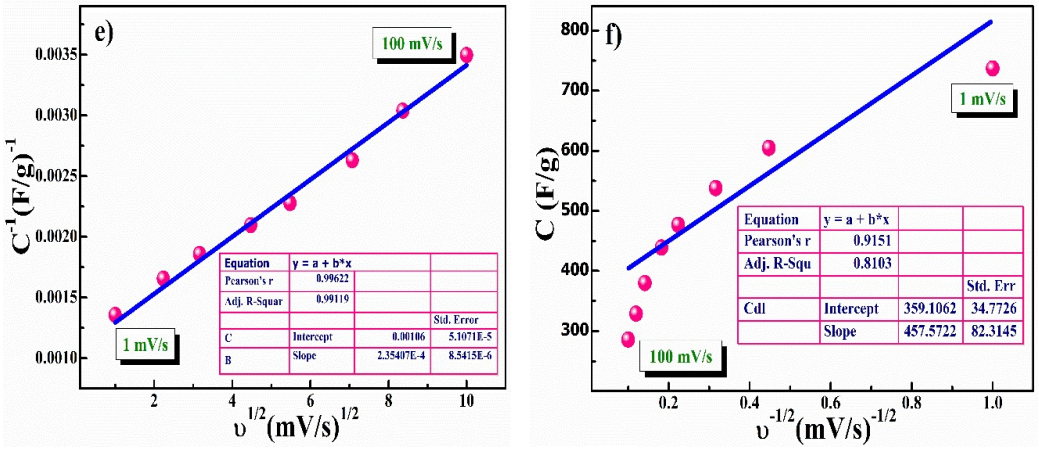

Figure 4.6 (e, f) Corresponding to Trasatti plot at different scan rates

The charge storage on the electrode depends on the scan rate. Fig. 4.6e shows the linear fit of C^{-1} vs. $\upsilon^{1/2}$ plot at different sweep rates, and the y-intercept in the plot represents the total capacitance of the electrode. Fig. 4.6f presents the linear fit of C vs. $\upsilon^{-1/2}$ plot and the y-intercept presents the electrode's outer surface charge storage. The total

capacitance value (C_{total}), using the Trassati plot, was found to be 943.4 F/g. Inner surface contribution (C_{in}) was found to be 584 F/g (62% of the total capacitance) and outer surface contribution (C_{out}) was found to be 359 F/g (38% of the total capacitance). Thus the nanosphere CoS electrodes store charge through both surface capacitive reactions and the diffusion-controlled intercalative charge storage process.

4.3.7.5 Chronoamperometry Charge/Discharge Analysis

Galvanostatic charge-discharge measurements in 2 M KOH aqueous electrolytes were carried out to gain a better understanding of the electrochemical properties of the CoS electrode. From equation 4.13, the specific capacitance of the electrode was determined from the galvanostatic charge-discharge curve. [11]

$$C\text{sp} = \frac{I\Delta t}{m\Delta V} \qquad (4.13)$$

Where I is the discharge current density (A), Δt is the discharge time (s), m is the mass of the CoS in the electrode (g) and ΔV is the potential window. As shown in Fig. 4.7a, specific capacitances of the electrode were obtained to 761, 685, 608, 506 and 381 F/g at the current densities of 1, 2, 3, 5 and 10 A/g, respectively. The specific capacitance decreases as current density increases. The specific capacitance decreases to ~50% of its initial value in the current density range of 1 to 10 A/g. Fig. 4.7b displays the charge storage stability of the electrode and Fig. 4.7c exhibits the long-term cyclic performances of the CoS electrode at 10 A/g for 10000 cycles. 83.5% capacity retention indicates the stability of the CoS nanospheres electrode after 10000 cycles. The superior reversibility of the electrode is further displayed as the electrode's coulombic efficiency $\left(\eta = {}^{t_d}/_{t_c}\right)$ was 93% after 10000 cycles of continuous charge/discharge.

Fig. 4.7d shows the comparative study of GCD at 0.5, 1, 2 and 4 M KOH concentrations. It is clear from the discharge time that the electrode delivers a longer discharge time in 2 M KOH electrolytes compared to 0.5, 1 and 4 M KOH electrolytes at a 1 A/g current rate. The specific capacitance of the electrode was calculated from the charge-discharge curve and is 547, 622, 761 and 718 F/g for 0.5, 1, 2 and 4 M KOH electrolyte concentrations, respectively. From comparative GCD observations, an increase in specific capacitance value from 0.5 to 2 M KOH concentration and then a decrease in capacitance at 4 M KOH concentration is confirmed which is in fair agreement with the results of the CV study.

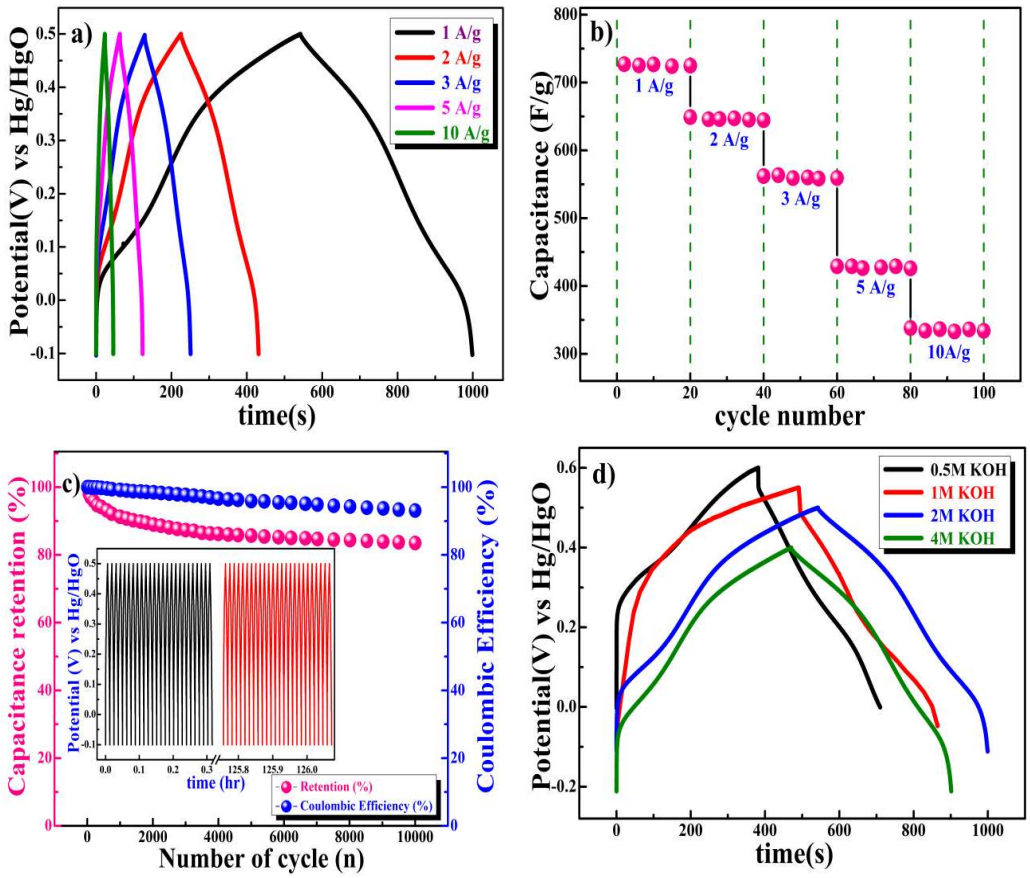

Fig. 4.7 (a) Galvanostatic charge/discharge (GCD) curve of the CoS electrode, **(b)** Capacitance performance of the CoS electrode at various current densities, **(c)** Capacitance retention and coulombic efficiency of the CoS electrode and **(d)** Comparative study of GCD at different electrolyte concentration.

4.3.7.6 Analysis of Electrochemical Impedance Spectroscopy (EIS)

Electrochemical impedance spectroscopy (EIS) and the Nyquist plot combined with their equivalent circuit elements in the frequency range of 100 kHz to 0.1 Hz at 10 mV applied voltage are shown in Fig. 4.7e.

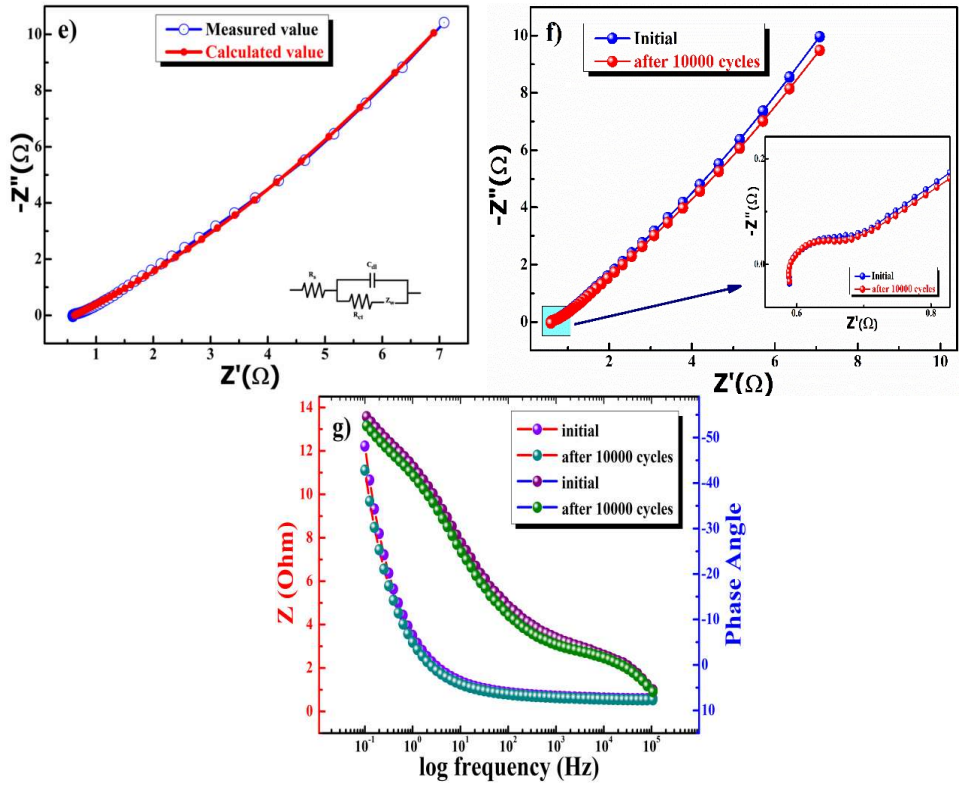

Fig. 4.7 (e) Fitted Nyquist plot, **(f)** Comparative Nyquist plot before and after long term cyclic stability and **(g)** Bode plot at 10 mV between 100 kHz - 0.1 Hz.

The specific impedance of the electrode was distributed over charge transfer resistance (R_{ct}), electric series resistance (R_s) and Warburg impedance (R_w). The R_s and R_{ct} values for the CoS electrode were found to be 0.62 and 0.73 Ω, respectively. Lower-frequency data represent the Warburg diffusion resistance for the CoS electrode. In order to investigate the detailed electrochemical characteristics of the CoS electrode before and after 10000 repeated charge-discharge cycles, EIS tests were carried out. Fig. 4.7f shows the resultant Nyquist plots before and after; spectra exhibits a depressed arc (in the inset) in the high-frequency range corresponding to faradaic reactions, followed by

a straight line in the low-frequency range, indicating a fast OH^- ion diffusion-controlled process. [24]

The EIS spectra show the good electrochemical stability of the CoS electrode after 10000 repeated charge-discharge cycles compared to the initial cycle. The Bode plot shown in Fig. 4.7g presents the phase angle with respect to the applied frequency. The change in phase angles of the CoS electrode from 54.8° to 52.6° was found after 10000 cycles of charge-discharge. The lower phase angle (around 50°) confirms the pseudocapacitive nature of charge storage on the CoS electrode. [35, 36]

4.3.7.7 Electrochemical Charge Storage Behaviour in Neutral Na_2SO_4 Electrolyte

Further, experiments were carried out to examine the capacitance of the CoS electrodes in a neutral 0.5 M Na_2SO_4 electrolyte. The CV plots at various scan rates shown in Fig. 4.8a represent the EDLC-type behavior in the majority as redox peaks completely disappear at high scan rates. Specific capacitance, which is the function of scan rate, estimated for the CoS electrode for 0.5 M Na_2SO_4 electrolyte are 291, 246, 189, 137, 114, 82, 51 and 43 F/g at 1, 2, 5, 10, 30, 50, 70 and 100 mVs^{-1} scan rates respectively. Fig. 4.8b displays the galvanostatic charge/discharge capacitance of the electrode and the capacitance was found to be 283, 220, 171, 123 and 57 F/g at 1, 2, 3, 5 and 10 A/g, respectively. Fig. 4.8c shows the comparative CV plots of the CoS electrode in neutral 0.5 M Na_2SO_4 and basic 2 M KOH electrolytes. The radius of the ionic hydration sphere of the electrolytes, and the conductivity and mobility of the ions are likely to be responsible for the variations in the current response and CV characteristics in different electrolytes. Ionic properties of the KOH and Na_2SO_4 aqueous electrolytes are listed in Table 4.1. [37]

Table 4.1 Ionic properties of the aqueous electrolytes [21] [38]

Ions	Radius of hydration sphere (Å)	Mol. conduct. (S m^2 mol^{-1})	Ionic mobility (cm^2 s^{-1} v^{-1})
OH^-	3.00	1.98×10^{-2}	20.60×10^{-5}
SO_4^{2-}	3.79	0.8×10^{-2}	8.30×10^{-5}

There were changes in the redox peaks from KOH to Na_2SO_4 electrolyte. The redox peaks in 2 M KOH were found to be more dominant than those in 0.5 M Na_2SO_4; this may be due to the size difference between the hydration radii of hydroxyl ions (3 Å) and sulfate ions (3.79 Å).

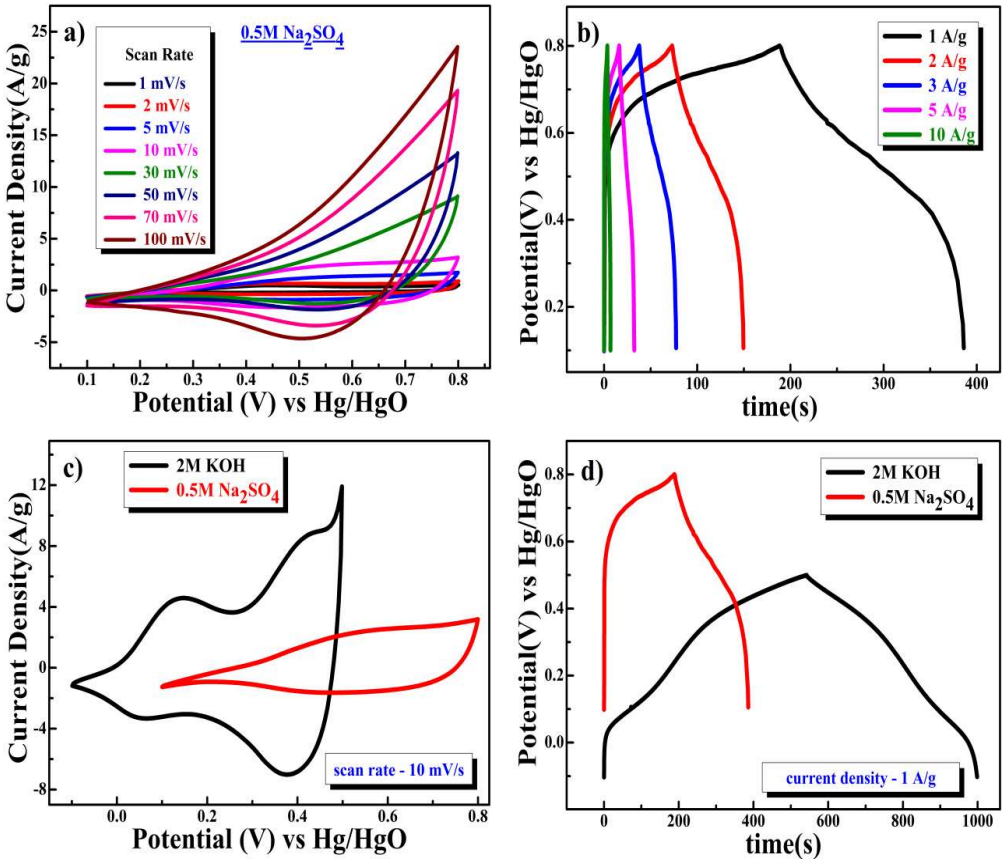

Fig. 4.8 (a) CV and **(b)** GCD plot in 0.5 M Na_2SO_4 electrolyte, **(c)** Comparative CV plot in 2 M KOH and 0.5 M Na_2SO_4 electrolyte at the scan rate of 10 mV/s and **(d)** Comparative charge/discharge plot in 2 M KOH and 0.5 M Na_2SO_4 electrolyte at the current density of 1 A/g of the CoS electrode.

The number of ions that diffused through the pores is decreased as bigger SO_4^{2-} hydrate spheres have limited mobility in the pores of the electrode that results in slow diffusion and lowering the formation of electric double layers. The greater conductivity of the OH^- ion (1.98×10^{-2} S m^2 mol^{-1}) in the KOH electrolyte compared to SO_4^{2-} (0.8×10^{-2} S m^2 mol^{-1}) in Na_2SO_4 exhibits a superior current response in the CV curve. [38],[39] GCD experiments were carried out in neutral 0.5 M Na_2SO_4 and basic 2 M KOH electrolytes to determine the electrode's charge storage capabilities in different electrolytes. Fig. 4.8d shows that the electrode delivers a longer discharge time in KOH electrolyte compared to Na_2SO_4 electrolyte at the current density of 1 A/g. These studies confirm the suitability of aqueous 2 M KOH electrolytes for superior electrode performance.

4.3.7.8 Asymmetric Full Cell Test of CoS //AC (CV, GCD, and Cyclic Stability)

Two electrode measurements in 2 M KOH were fabricated to comprehend the charge storage behavior of the CoS electrode employing AC as a counter electrode. The specific capacitance of the positive and negative electrodes must be balanced using equation 4.14 to obtain the maximum specific capacitance of the full cell.

$$\frac{1}{C_{total}} = \frac{1}{C_{positive}} + \frac{1}{C_{negative}} \tag{4.14}$$

To balance the cell's capacity to store charges, the mass ratio (m^+/m^-) of the positive and negative electrodes was determined using Equation 4.15.

$$\frac{m^+}{m^-} = \frac{C_- \times \Delta E_-}{C_+ \times \Delta E_+} \tag{4.15}$$

m^+,m^-, C_+, C_-, ΔE_+, ΔE_- are mass, specific capacitance, and potential window of positive and negative electrodes obtained from three-electrode CV measurements. [40]

Separate CV curves for the CoS nanosphere electrode and AC (negative electrode) are shown in a single operating potential window range at a scan rate of 10 mV/s. As AC is used to increase the conductivity of the active electrode, when calculating the electrochemical charge storage capacity of the CoS electrode, the contribution in capacitance due to the AC electrode is extracted and the obtained data shows only the capacitive value of the CoS electrode. Therefore, the calculated mass ratio (m^+/m^-) of CoS electrode to AC was approximately 1.2:1 for the asymmetric cell. SCs must be applicable in the field to evaluate their potential for going from the lab to the market. Therefore, SCs need to be investigated within the parameters of commercial supercapacitors (mass loading of 10 mg/cm^2) to recognize their place in a larger picture

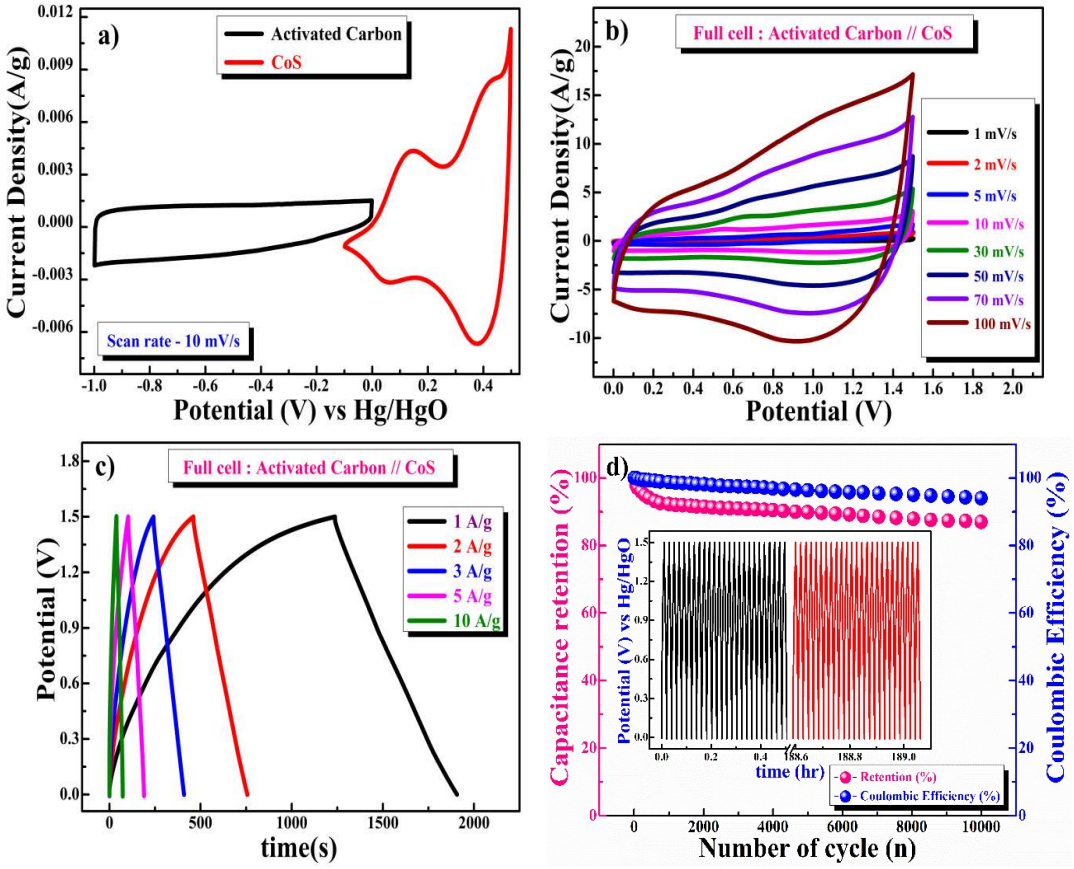

Fig. 4.9 (a) Separate CV plots for AC and CoS electrode in 2 M KOH Electrolyte 10 mV/s, **(b)** CV and **(c)** GDC of the full cell in HSC mode at different current rates and **(d)** Capacitance retention and coulombic efficiency.

of commercially employed SCs. [3] Fig. 4.9b shows the CV plot of a two-electrode HSC with a CoS electrode//AC asymmetry supercapacitor cell at scan rates ranging from 1 to 100 mVs^{-1} in the potential window 0 to 1.5 V. GCD profile of the full cell at different current densities is shown in Fig. 4.9c. The specific capacitances of HSCs calculated from GCD curves were found to be 447, 395, 334, 290 and 227 F/g at constant current densities of 1, 2, 3, 5 and 10 A/g, respectively.

As illustrated in Fig. 4.9d, the CoS//AC full cell in the form of an asymmetric supercapacitor full cell exhibits outstanding long-term cycling stability with retention of 87% capacitance of the full cell after 10000 cycles. CoS electrode//AC full cell also showed superior stability as the coulombic efficiency full cell in HSC mode is decreased only by 6% of its initial value after 10000 cycles.

4.3.7.9 Electrochemical Impedance Spectroscopy (EIS) of CoS//AC Full Cell

Fig. 4.9e and 4.9f present the EIS (Nyquist and Bode) plots in the frequency range of 100 kHz to 0.1 Hz at 10 mV applied potential, showing the superior charge transfer rates, and higher specific capacitance of the CoS electrode//AC full cell in HSC mode.

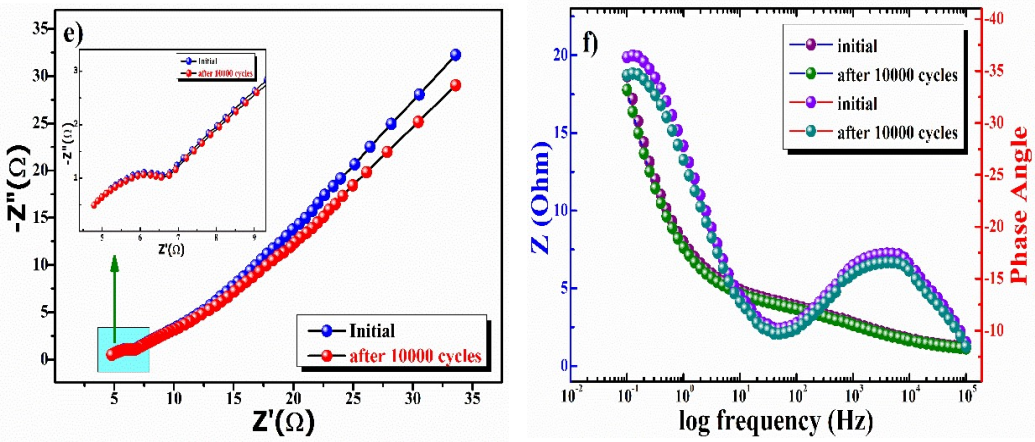

Fig. 4.9 (e) Nyquist and **(f)** Bode plot at 10 mV at initial cycle and after 10000 cycle of full cell formation.

However, a slight decrease in capacity is due to the partially irreversible nature of the electrode, which was observed during the cycling test. The EIS result also confirms the superior cycling stability of the full cell by demonstrating a slight change in the cell's internal and charge transfer resistances before and after the long-term cycling stability test.

4.3.7.10 Study of Energy Density vs Power Density of CoS //AC full cell

The power and energy density of full-cell asymmetric supercapacitors were calculated using equations 4.16 & 4.17.

$$P(W/kg) = \frac{E \text{ X } 3600}{t_{dis}} \quad (4.16)$$

$$E(Wh/kg) = \frac{1}{2}\frac{C_{ASC}}{3.6}\Delta V^2 \quad (4.17)$$

C_{sp} is the specific capacitance of the full cell, ΔV is the operating voltage window, and $t_{dis}$is discharge time in GCD experiments. Fig. 4.9g presents the Ragone plot (energy density vs. power density) of the CoS//AC full-cell in HSC mode for comparison with other reported sulfide-based supercapacitors. The asymmetric full-cell supercapacitor attains the highest energy density equivalent of 139.7 Wh/kg and power density equivalent of 0.75 kW/kg at 1 A/g current density. At a higher current density (10 A/g), the maximum power density of the full cell reaches 7.51 kW/kg at the energy density of 70.9 Wh/kg. Table 4.2 highlights a literature survey of different nanostructured sulfide-based electrodes for supercapacitor applications, e.g., specific capacitance, capacity retention, energy, and power density.

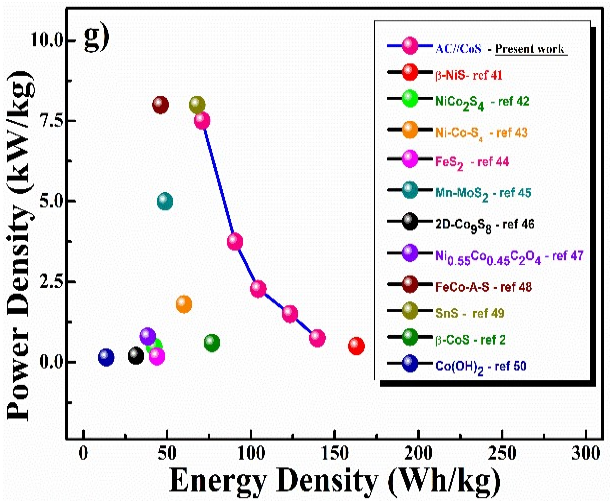

Fig. 4.9 (g) Ragone plot of the CoS//AC full cell in HSC mode in comparison with reported supercapacitor devices.

Table 4.2 The performances of the CoS//AC full cell in HSC mode compared with other reported full cell supercapacitors.

Material	**Energy density (Wh/kg)**	**Power density (kW/kg)**	**Cycling stability (%) after "n" cycles**	**Capacitance (F/g)**	**Ref.**
β -NiS	163	0.5	90.0%, 2500	780 at 1 A/g	[41]
$NiCo_2S_4$ spheres	42.3	0.48	78.6%, 10000	119.1 at 5 mV/s	[42]
Ni-Co-S_4	60	1.8	90.1%, 10000	133 at 2 mV/s	[43]
FeS_2 nanospheres	44	0.18	97.0%, 5000	484 at 5 mV/s	[44]
Mn-MoS_2	48.8	5	77.0%, 5000	135 at 5 mV/s	[45]
2D- Co_9S_8	31.4	0.2	90.0%, 5000	82.9 at 1 A/g	[46]
$Ni_{0.55}Co_{0.45}C_2O_4$	38.5	0.8	80.0%, 10000	108 at 1 A/g	[47]
FeCo-A-S	46.1	8	79.3%, 10000	2932.2 at 1 A/g	[48]
MnS thin films	18.9	0.25	75.0%, 2000	68.3 at 3 mA cm^{-2}	[49]
CoS-AC//AC	44.2	0.4	77.5%, 2000	117.5 at 1 A/g	[2]
$Co(OH)_2$	13.6	0.15	80.0%, 5000	38.9 at 2 A/g	[50]
CoS nano-sphere	**139.7 123.4 104.4 90.6 70.9**	**0.75 1.5 2.28 3.75 7.51**	**87.0%, 10000**	**447 at 1 A/g**	**Present work**

4.4 Conclusions

In summary, the single-phase hexagonal CoS nano-sphere was synthesized using a simple H_2S-mediated one-pot synthesis route in the aqueous medium. Slow diffusion of H_2S gas into the water resulted in the formation of single-phase nanocrystalline CoS nano-spheres. The XRD pattern confirms the precipitation of a single-phase hexagonal CoS nano-spheres and the crystallite size calculated using the Debye Scherrer equation was found to be ~18 nm. CoS nano-sphere shows the quantum confinement effect due to the smaller/nanocrystalline size of the particles by Raman spectra and supported by XRD and UV-Visible spectroscopy data. The CoS electrode showed highly pseudocapacitive performance with a specific capacitance of 776 F/g at 1 mVs^{-1} in a potential window of -0.1 to 0.5 V in CV and 761 F/g at a current density of 1 A/g in the potential window of -0.1 to 0.5 V in GCD measurement. A predominant redox-mediated diffusion-controlled intercalative charge storage mechanism seems to be operative behind the superior capacitance of the electrode, as the diffusion-controlled (inner) and surface (outer) charges stored by the CoS electrodes were found to be 62% and 38%, respectively. In 2 M KOH electrolyte, CoS//AC full cell asymmetric supercapacitor resulted in power density equivalent to 0.75 kW/kg at the energy density of 139.7 Wh/kg in the voltage window of 1.5 V in 2 M KOH electrolyte at 1 A/g current density. Electrochemical performances of the CoS nanosphere indicate that the capacitance value and charge storage behavior of the CoS nanosphere electrode are comparable to or better than most transition-metal nanostructured pseudocapacitors studied recently. These results show that the CoS nano-sphere can be used as a pseudocapacitive electrode in asymmetric hybrid supercapacitor mode for large-scale energy storage applications.

4.5 References

1. Kulkarni, P., et al., *Nanostructured binary and ternary metal sulfides: synthesis methods and their application in energy conversion and storage devices.* Journal of Materials Chemistry A, 2017. **5**(42): p. 22040-22094.
2. Xu, T., et al., *One-pot synthesis of a CoS-AC electrode in a redox electrolyte for high-performance supercapacitors.* Journal of Applied Electrochemistry, 2019. **49**: p. 1069-1077.
3. Das, A., et al., *Performance and future directions of transition metal sulfide-based electrode materials towards supercapacitor/supercapattery.* Wiley Interdisciplinary Reviews: Energy and Environment, 2022. **11**(1): p. e414.
4. Chandrasekaran, S., et al., *Recent advances in metal sulfides: from controlled fabrication to electrocatalytic, photocatalytic and photoelectrochemical water splitting and beyond.* Chemical Society Reviews, 2019. **48**(15): p. 4178-4280.
5. Toe, C.Y., et al., *Recent advances and the design criteria of metal sulfide photocathodes and photoanodes for photoelectrocatalysis.* Journal of Materials Chemistry A, 2021. **9**(36): p. 20277-20319.
6. Chen, G.Z., *Understanding supercapacitors based on nano-hybrid materials with interfacial conjugation.* Progress in Natural Science: Materials International, 2013. **23**(3): p. 245-255.
7. Justin, P. and G.R. Rao, *CoS spheres for high-rate electrochemical capacitive energy storage application.* International Journal of Hydrogen Energy, 2010. **35**(18): p. 9709-9715.
8. Dong, W., et al., *Hydrothermal synthesis and structure evolution of hierarchical cobalt sulfide nanostructures.* Dalton Transactions, 2011. **40**(1): p. 243-248.

9. Geng, P., et al., *Transition metal sulfides based on graphene for electrochemical energy storage.* Advanced Energy Materials, 2018. **8**(15): p. 1703259.

10. Wu, L., et al., *Cobalt Sulfide Nanotubes (Co9S8) Decorated with Amorphous MoS x as Highly Efficient Hydrogen Evolution Electrocatalyst.* ACS Applied Nano Materials, 2018. **1**(3): p. 1083-1093.

11. Lin, J.-Y. and S.-W. Chou, *Cathodic deposition of interlaced nanosheet-like cobalt sulfide films for high-performance supercapacitors.* Rsc Advances, 2013. **3**(6): p. 2043-2048.

12. Wang, Y., et al., *Physical confinement and chemical adsorption of porous C/CNT micro/nano-spheres for CoS and Co9S8 as advanced lithium batteries anodes.* Electrochimica Acta, 2019. **299**: p. 489-499.

13. Luo, F., et al., *Rapid synthesis of three-dimensional flower-like cobalt sulfide hierarchitectures by microwave assisted heating method for high-performance supercapacitors.* Electrochimica Acta, 2014. **123**: p. 183-189.

14. Kumar, N., N. Raman, and A. Sundaresan, *Synthesis and properties of cobalt sulfide phases: CoS2 and Co9S8.* Zeitschrift für anorganische und allgemeine Chemie, 2014. **640**(6): p. 1069-1074.

15. Qu, B., et al., *β-Cobalt sulfide nanoparticles decorated graphene composite electrodes for high capacity and power supercapacitors.* Nanoscale, 2012. **4**(24): p. 7810-7816.

16. Muradov, M.B., et al., *Synthesis and characterization of cobalt sulfide nanoparticles by sonochemical method.* Infrared Physics & Technology, 2018. **89**: p. 255-262.

17. Abza, T., et al., *Characterization of cobalt sulfide thin films synthesized from acidic chemical baths.* Advances in Materials Science and Engineering, 2020. **2020**: p. 1-9.

18. Qu, P., et al., *Nanoflower-like CoS-decorated 3D porous carbon skeleton derived from rose for a high performance nonenzymatic glucose sensor.* RSC advances, 2015. **5**(129): p. 106661-106667.

19. Ju, S., et al., *In situ surface chemistry engineering of cobalt-sulfide nanosheets for improved oxygen evolution activity.* ACS Applied Energy Materials, 2019. **2**(6): p. 4439-4449.

20. Yang, H., et al., *Sphere-like CoS with nanostructures as peroxidase mimics for colorimetric determination of H 2 O 2 and mercury ions.* RSC advances, 2016. **6**(71): p. 66963-66970.

21. Guillaume, F., et al., *Optical phonons in millerite (NiS) from single-crystal polarized Raman spectroscopy.* Journal of Raman Spectroscopy: An International Journal for Original Work in all Aspects of Raman Spectroscopy, Including Higher Order Processes, and also Brillouin and Rayleigh Scattering, 2008. **39**(10): p. 1419-1422.

22. Ramachandran, R., et al., *Synthesis of cobalt sulfide–graphene (CoS/G) nanocomposites for supercapacitor applications.* IEEE transactions on nanotechnology, 2013. **12**(6): p. 985-990.

23. Behnoudnia, F. and H. Dehghani, *Anion effect on the control of morphology for NiC 2 O 4· 2H 2 O nanostructures as precursors for synthesis of Ni (OH) 2 and NiO nanostructures and their application for removing heavy metal ions of cadmium (II) and lead (II).* Dalton Transactions, 2014. **43**(9): p. 3471-3478.

24. Mishra, N.K., et al., *NiC2O4· 2H2O Nanoflakes: A Novel Redox-mediated Intercalative Pseudocapacitive Electrode for Supercapacitor Applications in Aqueous KOH and Neutral Na2SO4 electrolytes.* ChemistrySelect, 2022. **7**(21): p. e202201134.

25. Wang, Y.-K., et al., *3D hierarchically structured CoS nanosheets: Li+ storage mechanism and application of the high-performance lithium-ion capacitors.* ACS applied materials & interfaces, 2019. **12**(3): p. 3709-3718.

26. Kumar, K.A., et al., *Effect of bi-functional hierarchical flower-like CoS nanostructure on its interfacial charge transport kinetics, magnetic and electrochemical behaviors for supercapacitor and DSSC applications.* Scientific reports, 2019. **9**.

27. Gupta, A., et al., *SrFeO 3− δ: a novel Fe 4+↔ Fe 2+ redox mediated pseudocapacitive electrode in aqueous electrolyte.* Physical Chemistry Chemical Physics, 2022. **24**(18): p. 11066-11078.

28. Evanko, B., et al., *Redox-enhanced electrochemical capacitors: status, opportunity, and best practices for performance evaluation.* ACS Energy Letters, 2017. **2**(11): p. 2581-2590.

29. Mayedwa, N., et al., *Green synthesis of zin tin oxide (ZnSnO3) nanoparticles using Aspalathus Linearis natural extracts: Structural, morphological, optical and electrochemistry study.* Applied Surface Science, 2018. **446**: p. 250-257.

30. Su, D., et al., *High-capacity aqueous potassium-ion batteries for large-scale energy storage.* Advanced Materials, 2017. **29**(1): p. 1604007.

31. Fleischmann, S., et al., *Pseudocapacitance: from fundamental understanding to high power energy storage materials.* Chemical Reviews, 2020. **120**(14): p. 6738-6782.

32. Ardizzone, S., G. Fregonara, and S. Trasatti, *"Inner" and "outer" active surface of RuO2 electrodes.* Electrochimica Acta, 1990. **35**(1): p. 263-267.

33. Wang, J., et al., *Pseudocapacitive contributions to electrochemical energy storage in TiO2 (anatase) nanoparticles.* The Journal of Physical Chemistry C, 2007. **111**(40): p. 14925-14931.

34. Kim, H.-S., et al., *Oxygen vacancies enhance pseudocapacitive charge storage properties of MoO3− x.* Nature materials, 2017. **16**(4): p. 454-460.

35. Mohanadas, D., et al., *Facile synthesis of PEDOT-rGO/HKUST-1 for high performance symmetrical supercapacitor device.* Scientific reports, 2021. **11**(1): p. 11747.

36. Krishnamoorthy, K., et al., *One pot hydrothermal growth of hierarchical nanostructured Ni3S2 on Ni foam for supercapacitor application.* Chemical Engineering Journal, 2014. **251**: p. 116-122.

37. Wu, H., et al., *The effects of electrolyte on the supercapacitive performance of activated calcium carbide-derived carbon.* Journal of power sources, 2013. **226**: p. 202-209.

38. Mohd Hanappi, M.F.Y., et al., *Influence of aqueous KOH and H2SO4 electrolytes ionic parameters on the performance of carbon-based supercapacitor electrodes.* Functional Materials Letters, 2017. **10**(03): p. 1750013.

39. Pal, B., et al., *Electrolyte selection for supercapacitive devices: a critical review.* Nanoscale Advances, 2019. **1**(10): p. 3807-3835.

40. Subramani, K., et al., *All-solid-state asymmetric supercapacitors based on cobalt hexacyanoferrate-derived CoS and activated carbon.* RSC advances, 2017. **7**(11): p. 6648-6659.

41. Kushwaha, V., et al., *Nanocrystalline β-NiS: a redox-mediated electrode in aqueous electrolyte for pseudocapacitor/supercapacitor applications.* Physical Chemistry Chemical Physics, 2023. **25**(1): p. 555-569.

42. Shen, L., et al., *Formation of nickel cobalt sulfide ball-in-ball hollow spheres with enhanced electrochemical pseudocapacitive properties.* Nature communications, 2015. **6**(1): p. 6694.

43. Chen, W., C. Xia, and H.N. Alshareef, *One-step electrodeposited nickel cobalt sulfide nanosheet arrays for high-performance asymmetric supercapacitors.* ACS nano, 2014. **8**(9): p. 9531-9541.

44. Javed, M.S., et al., *A high-performance flexible solid-state supercapacitor based on Li-ion intercalation into tunnel-structure iron sulfide.* Electrochimica Acta, 2016. **219**: p. 742-750.

45. Singha, S.S., et al., *Mn incorporated MoS2 nanoflowers: A high performance electrode material for symmetric supercapacitor.* Electrochimica Acta, 2020. **338**: p. 135815.

46. Rakhi, R., et al., *Nanostructured cobalt sulfide-on-fiber with tunable morphology as electrodes for asymmetric hybrid supercapacitors.* Journal of Materials Chemistry A, 2014. **2**(38): p. 16190-16198.

47. Wang, L., et al., *Interfacial synthesis of micro-cuboid Ni0. 55Co0. 45C2O4 solid solution with enhanced electrochemical performance for hybrid supercapacitors.* Nanoscale, 2019. **11**(29): p. 13894-13902.

48. Yan, S.-x., et al., *Asymmetric, flexible supercapacitor based on Fe–Co Alloy@ sulfide with high energy and power density.* ACS Applied Materials & Interfaces, 2021. **13**(42): p. 49952-49963.

49. Pujari, R., et al., *Synthesis of MnS microfibers for high performance flexible supercapacitors.* Materials & Design, 2016. **108**: p. 510-517.

50. Tang, Y., et al., *Morphology controlled synthesis of monodisperse cobalt hydroxide for supercapacitor with high performance and long cycle life.* Journal of Power Sources, 2014. **256**: p. 160-169.